Pressure-induced commensurate order in TbMn 2 O 5 and DyMn 2 O 5 : Influence of rare-earth anisotropy and 3 d − 4 f exchange

M. Deutsch, W. Peng, P. Foury-Leylekian, V. Balédent, S. Chattopadhyay, M. T Fernandez-Diaz, T. C Hansen, A. Forget, D. Colson, M. Greenblatt, et al.

Pressure-induced commensurate order in $TbMn_2O_5$ and $DyMn_2O_5$: Influence of rare-earth anisotropy and $3d$-$4f$ exchange

M. Deutsch,[1,2] W. Peng,[3] P. Foury-Leylekian,[3] V. Balédent,[3] S. Chattopadhyay,[4] M. T. Fernandez-Diaz,[5] T. C. Hansen,[5] A. Forget,[6] D. Colson,[6] M. Greenblatt,[7] M.-B. Lepetit,[8,5] S. Petit,[2] and I. Mirebeau[2,*]

[1]*Université de Lorraine, CNRS, CRM2, F-54000 Nancy, France*

[2]*LLB, CEA, CNRS, Université Paris-Saclay, Centre de Saclay, F-91191 Gif-sur Yvette, France*

[3]*Laboratoire de Physique des Solides, Université Paris-Sud, CNRS-UMR 8502, 91405 Orsay Cedex, France*

[4]*Hochfeld-Magnetlabor Dresden (HLD-EMFL), Helmholtz-Zentrum Dresden-Rossendorf, 01328 Dresden, Germany*

[5]*Institut Laue Langevin, 71 Avenue des Martyrs CS 20156, 38042 Grenoble Cedex 9, France*

[6]*Service de Physique de l'Etat Condensé, CEA, Université Paris-Saclay, Centre de Saclay, F-91191 Gif-sur Yvette France*

[7]*Department of Chemistry and Chemical Biology, Rutgers, the State University of New Jersey, Piscataway, New Jersey 08854, USA*

[8]*Institut Néel, CNRS UPR 2940, Boîte Postale 166, 38042 Grenoble Cedex 9, France*

(Received 20 April 2018; published 10 July 2018)

The magnetic structure of $TbMn_2O_5$ and $DyMn_2O_5$ multiferroics has been studied by high-pressure neutron diffraction in a large pressure range up to 6.6 GPa. In both cases, we observe a pressure-induced commensurate magnetic phase with propagation vector $(\frac{1}{2}\ 0\ \frac{1}{2})$, growing with pressure at the expense of the ambient pressure phases. Being previously observed in YMn_2O_5 and $PrMn_2O_5$, this phase is most likely a generic feature of the RMn_2O_5 multiferroic family. A simple model is proposed to explain qualitatively the emergence of this pressure-induced phase. Differences between $TbMn_2O_5$ and $DyMn_2O_5$ behaviors at ambient and low pressures provide clues on the interaction scheme.

DOI: 10.1103/PhysRevB.98.024408

I. INTRODUCTION

Multiferroics attract a renewed interest as potential devices in spintronics or data storage. The coupling between magnetic and electric order parameters is a promising tool to manipulate magnetic properties via an electric field or vice versa. The strongest effects have been observed in improper multiferroics, such as $RMnO_3$ and RMn_2O_5 families, where R is a rare-earth ion Y or Bi. In these compounds, ferroelectricity appears only in the ordered magnetic state, calling for a strong interplay among spin, charge, orbital, and lattice degrees of freedom [1]. In RMn_2O_5 the nature of the spin-lattice coupling has been extensively debated, and two main mechanisms are usually invoked. The inverse Dzyaloshinskii-Moryia (DM) interaction [2], at play for noncollinear magnetic structures, assumes that the cycloidal order breaks the inversion symmetry by inducing atomic displacements to minimize the DM energy. In collinear antiferromagnetic states, charge order and electric polarization can occur when atoms are slightly displaced by exchange striction. It seems that either one or the other mechanism may dominate, depending on the compound or temperature range considered [1,3–8]. The relative roles of such mechanisms in the low-temperature spin order ferroelectricity are actively investigated in the series [9–12].

In these frustrated systems, the magnetic structures are complex and show a large variety of magnetic arrangements, depending on the R ion and on the temperature. For a given ion, the compound usually undergoes a cascade of magnetic transitions giving rise to commensurate or incommensurate magnetic structures [13,14]. The sequence of succession of those magnetic phases is shown in Fig. 1 for $TbMn_2O_5$.

In RMn_2O_5, the magnetic structures show a large variety of periodicities as shown by the numerous propagation vectors reported in literature (see Table I). The details of the ordering have been highly debated in literature [3,5–7,15–17], but as a global feature, magnetic ordering can be described by coupled antiferromagnetic (AF) chains of Mn moments, yielding a $k_x = \frac{1}{2}$ component of the propagation vector for most of them. Furthermore, these moments generally lie on the (a,b) plane (see Fig. 3). The wide diversity observed for the k_z component remains, however, puzzling, and the interaction scheme at play stabilizing $k_z = 0, 1/4, 1/2$, or an incommensurate k_z is still an issue [13,18–20].

In this paper, we address this question and pursue the idea that applying pressure is a good tool to unveil the mechanisms at the origin of these behaviors on a macroscopic scale [16,21] or microscopic one [22,23]. Previous neutron-diffraction studies on YMn_2O_5 and $PrMn_2O_5$ under high pressure have shown the onset of a pressure-induced commensurate phase (PCM), which appears at low pressure and progressively develops as pressure increases at the expense of both the ambient pressure CM and the ICM phases [22–24]. The PCM phase propagation vector $\mathbf{k} = (\frac{1}{2}\ 0\ \frac{1}{2})$ is the same as in $BiMn_2O_5$ at ambient pressure. Since this pressure-induced phase may also play a crucial role in the anomalous variation of the electric polarization and dielectric constant with pressure and temperature [16,21], we have searched for it in other compounds of the family. In this paper we show that this PCM phase indeed exists in $TbMn_2O_5$ and $DyMn_2O_5$, suggesting that it is a rather general feature of

*isabelle.mirebeau@cea.fr

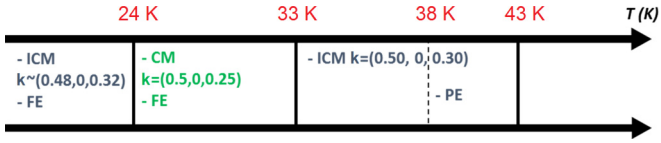

FIG. 1. Sequence of phases observed in $TbMn_2O_5$: With decreasing temperature, a transition from a paramagnetic to an incommensurate spin structure occurs at T_{N1} (43 K). The incommensurate (ICM) modulation is along (a,b), and $TbMn_2O_5$ remains paraelectric in this range. Below T_{C1} (33 K), a transition to a commensurate (CM) magnetic phase is observed. The propagation vector is $\mathbf{k} = (\frac{1}{2}\,0\,\frac{1}{4})$, and $TbMn_2O_5$ becomes ferroelectric. At T_{C2} (24 K), a third transition back to an ICM structure occurs with $\mathbf{k} = (\frac{1}{2}+\delta\,0\,\frac{1}{4}+\epsilon)$.

the RMn_2O_5 series. We discuss the interaction scheme which could lead to the emergence of this phase and its consequences on the pressure-induced magnetic phase diagram.

II. EXPERIMENT

Polycrystalline $TbMn_2O_5$ was prepared by a solid-state reaction from a stoichiometric mixture of Tb_2O_3 (99.99%) and Mn_2O_3 (99%). The powder was heated for 18 h four times from 1050 to 1085 °C under oxygen flux, cooled down to room temperature, and reground after each calcination. The polycrystalline $DyMn_2O_5$ was prepared by a precursor-based flux following a method described in Refs. [25,26]. We used isotope-enriched (^{163}Dy) to decrease the neutron absorption. The powder neutron-diffraction (PND) patterns were measured at ambient pressure on the high-resolution neutron diffractometer D2B of the Institut Laue Langevin [(ILL), Grenoble, France] with an incident wavelength λ of 1.59 Å.

The Tb sample was measured under pressure on the G6-1 diffractometer of the Laboratoire Léon Brillouin (LLB) (λ = 4.74 Å). We used a Cu-Be piston cylinder cell at pressures up to 1.2 GPa and a Kurchatov-LLB pressure cell [27] with sapphire anvils up to 3.4 GPa. The pressure cells were inserted in a helium cryostat, and the neutron patterns were collected down to 1.5 K for each pressure. Both Tb and Dy samples were measured under pressure on the high flux diffractometer

TABLE I. Magnetic propagation vectors observed in some RMn_2O_5 compounds, classified by increasing the atomic mass.

RMn_2O_5	Propagation vectors
Y	$\mathbf{k_1} = (\frac{1}{2}\,0\,\frac{1}{4})$ $\mathbf{k_2} = (\frac{1}{2}+\delta\,0\,\frac{1}{4}+\epsilon)$ $\mathbf{k_3} = (\frac{1}{2}\,0\,\frac{1}{4}+\gamma)$
La	$\mathbf{k_1} = (0\,0\,\frac{1}{2})$
Pr	$\mathbf{k_1} = (0\,0\,\frac{1}{2})$ $\mathbf{k_2} = (\frac{1}{2}\,0\,0)$
Nd	$\mathbf{k_1} = (\frac{1}{2}\,0\,0)$ $\mathbf{k_2} = (\frac{1}{2}\,0\,0.4-\delta)$
Sm	$\mathbf{k_1} = (\frac{1}{2}\,0\,0.327)$ $\mathbf{k_2} = (\frac{1}{2}\,0\,0.335)$ $\mathbf{k_3} = (\frac{1}{2}\,0\,0)$
Eu	$\mathbf{k_1} = (\frac{1}{2}\,0\,0)$
Tb	$\mathbf{k_1} = (\frac{1}{2}\,0\,\frac{1}{4})$ $\mathbf{k_2} = (\frac{1}{2}+\delta\,0\,\frac{1}{4}+\epsilon)$
Dy	$\mathbf{k_1} = (\frac{1}{2}\,0\,0)$ $\mathbf{k_2} = (\frac{1}{2}\pm\delta\,0\,\frac{1}{4}\pm\epsilon)$
Ho	$\mathbf{k_1} = (\frac{1}{2}\,0\,\frac{1}{4})$
Er	$\mathbf{k_1} = (\frac{1}{2}\,0\,\frac{1}{4})$
Bi	$\mathbf{k_1} = (\frac{1}{2}\,0\,\frac{1}{2})$

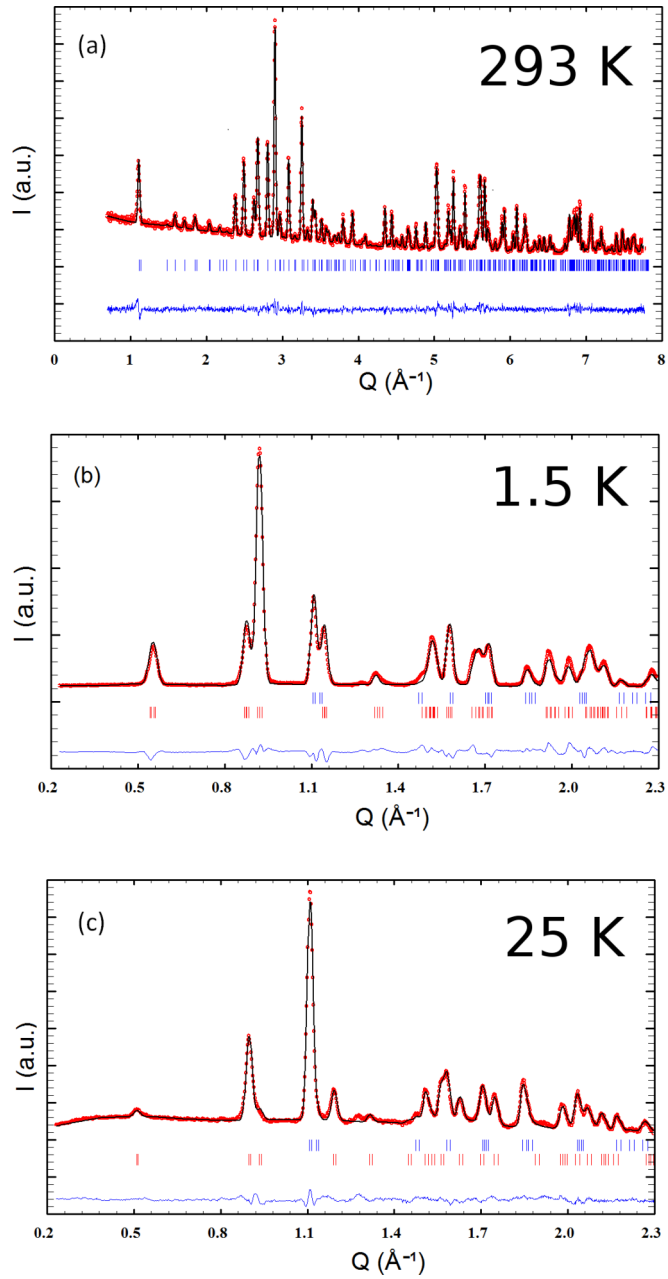

FIG. 2. $TbMn_2O_5$. Refined diffraction patterns measured at ambient pressure. (a) High-resolution pattern at ambient temperature; (b) $T = 1.5$ K; (c) $T = 25$ K. The patterns were refined with (b) LT-ICM and (c) CM phases, according to Ref. [33] for LT-ICM and Refs. [3,20] for CM. The solid black line is a FULLPROF refinement; the tick marks show the Bragg peak positions for the structural (blue) and magnetic (red) phases. The solid blue line is the difference between the calculated and the measured patterns.

D20 of the ILL (λ = 2.42 Å) [28]. We used a Paris-Edinburgh press combined with a close circle refrigerator with a minimum temperature of 3 K [29]. A Pb shave inserted in the powder was used as a pressure probe. The pressure was increased at ambient temperature when the pressure-transmitting medium (methanol/ethanol 4:1) is liquid to provide an isotropic pressure at low temperatures [30]. The PND patterns were collected versus temperature at 4.4 and 5.6 GPa for the Tb sample and at 2.4 and 6.6 GPa for the Dy sample.

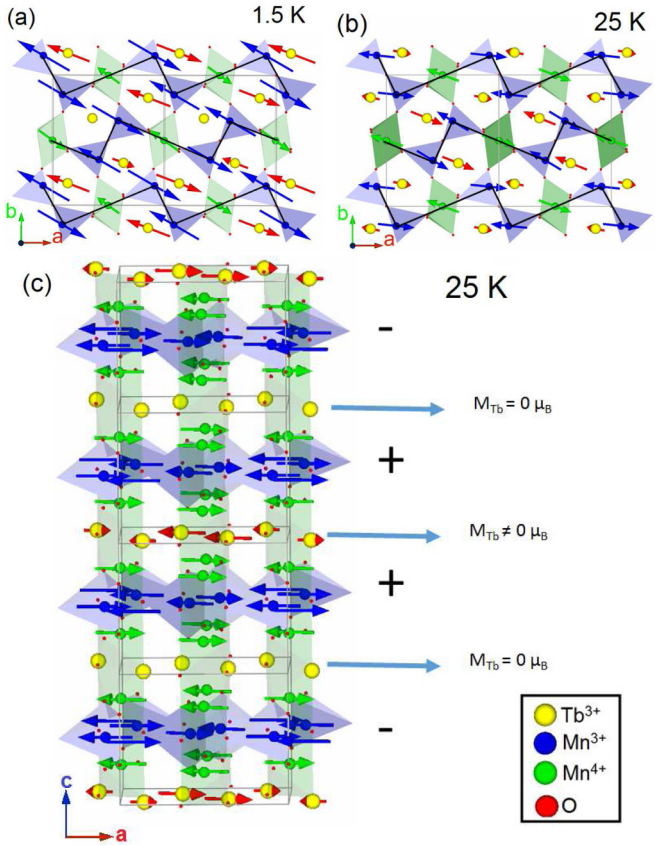

FIG. 3. $TbMn_2O_5$ refined magnetic structure. (a) at 1.5 K on the (a,b) plane; (b) at 25 K on the (a,b) plane; (c) at 25 K along the c axis. Mn^{3+} moments and Mn^{4+} moments form AF zigzag chains. The blue (respectively, green) arrows correspond to Mn^{3+} (respectively, Mn^{4+}) moments. The Tb moments (red arrows) have been reduced by a factor of 2 at 1.5 K for the sake of clarity. The black lines are guides for the eye.

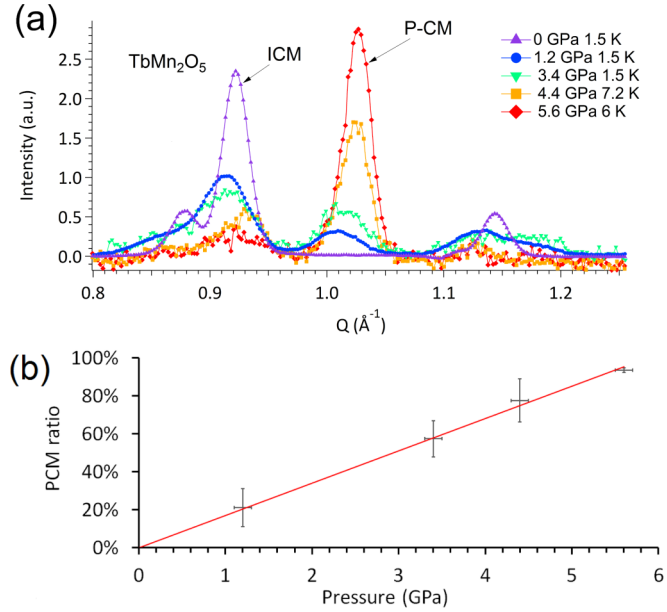

FIG. 4. $TbMn_2O_5$ (a) Magnetic patterns at low temperatures showing the onset of a PCM phase at the expense of the ambient pressure ICM phase. Patterns were normalized to a structural peak, and a pattern in the paramagnetic phase was subtracted. (b) Pressure dependence of the relative amount of the PCM phase around 5 K.

III. RESULTS AND ANALYSIS

A. $TbMn_2O_5$

The magnetic structures at ambient pressure are the starting point of the high-pressure data analysis. The PND patterns (Fig. 2) were refined using the FULLPROF suite [31] with results close to those previously published. In the CM phase, the Mn^{3+} and Mn^{4+} moments lie on the (a,b) plane where they form AF zigzag chains [Fig. 3(b)]. Along the c axis the Mn^{3+} and Mn^{4+} layers alternate in a "$-++-$" sequence. A small moment is induced on the Tb sites when adjacent Mn^{4+} layers are ferromagnetic whereas it is zero for an AF alignment [Fig. 3(c)]. The ICM phase also involves AF zigzag chains on the (a,b) plane but with an additional modulation along the a and c axes [Fig. 3(a)].

Under pressure, the lattice constants decrease, following an anisotropic compression law (see the Supplemental Material [32]). We observe at low temperatures the onset of new Bragg peaks [Fig. 4(a)], indexed with a propagation vector $\mathbf{k} = (\frac{1}{2}\ 0\ \frac{1}{2})$. They show the emergence of a PCM phase, similar to that observed in YMn_2O_5. When the pressure increases, the PCM phase clearly grows at the expense of the ambient pressure ICM phase [Fig. 4(a)]. From the relative peak intensities, we can estimate its relative amount versus pressure (see the Supplemental Material [32]). Importantly, diffraction patterns obtained with different pressure and neutron setups show the same tendency, namely, a linear increase in the PCM phase with increasing pressure [Fig. 4(b)].

Beyond 5.6 GPa and below 20 K, the PCM phase most likely exists as a single phase since all magnetic peaks are indexed with the same propagation vector $\mathbf{k} = (\frac{1}{2}\ 0\ \frac{1}{2})$, and we attempted to refine it [Fig. 5(a)]. Such refinement is delicate considering the small number of magnetic peaks and the 12 magnetic atoms belonging to three different sublattices. To limit the number of parameters we imposed several constraints: (i) We fixed the crystalline structure to the ambient pressure one and refined only the lattice parameters; (ii) we used the structure of the ambient pressure CM phase as a starting point; (iii) we considered planar configurations (as observed at ambient pressure) by varying the orientations of the Tb and Mn moments on the (a,b) plane. At 20 K, the Tb moments are small, and their orientation is difficult to determine, but at 6 K, we could clearly discard solutions with collinear (or almost collinear) Tb and Mn moments. In the refined magnetic structure [Fig. 5(b)] the Tb moments are oriented along the long axes of the oxygen pentagons, almost perpendicular to their neighboring Mn^{3+} and Mn^{4+} moments. As discussed in the Supplemental Material [32], such a structure involves a symmetry lowering from the space-group (SG) Pm [8] to SG $P1$. This symmetry lowering is undetectable on the crystal structure, at least, at our resolution level, but it may play a role by changing the energy balance of the magnetic interactions as discussed below.

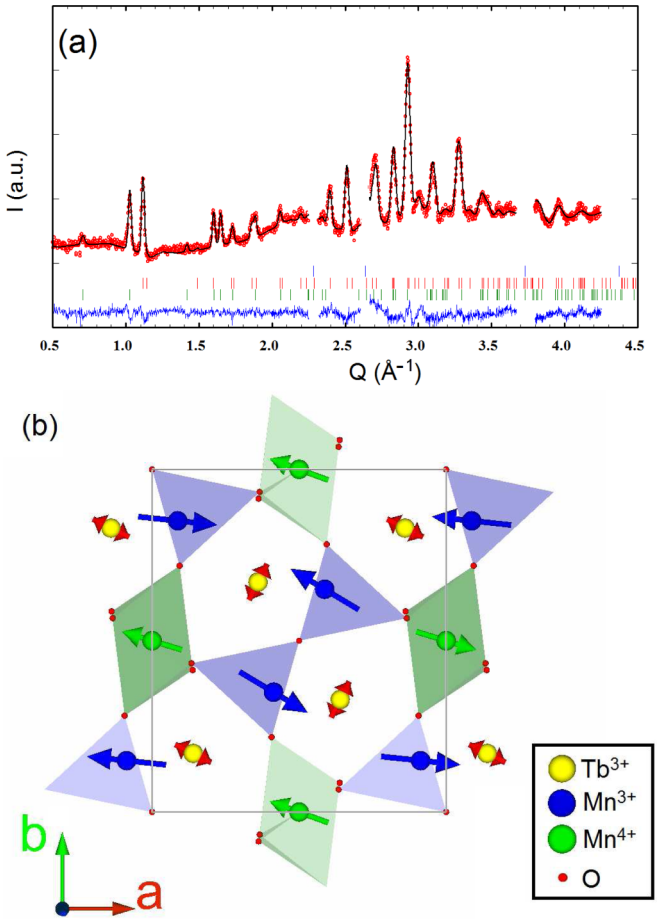

FIG. 5. $TbMn_2O_5$. (a) Refined pattern at 5.6 GPa and 20 K. Red ticks: structural peaks; green ticks: magnetic peaks. The blue ticks mark the position of the Pb structural peaks (not shown here) used to probe the pressure. (b) PCM structure. Mn^{3+}moments (blue arrows) and Mn^{4+} moments (green arrows) form AF zigzag chains. Tb moments are shown by red arrows.

B. $DyMn_2O_5$

At ambient pressure, $DyMn_2O_5$ undergoes a transition below $T_1 = 42$ K towards an ICM phase with a propagation vector $\mathbf{k}_1 = [\frac{1}{2}\,0\,\frac{1}{4} \pm \epsilon(T)]$. Below $T_2 = 8$ K, a first-order phase transition occurs from the ICM phase to a CM phase with $\mathbf{k}_2 = (\frac{1}{2}\,0\,0)$ [20,34–36] (see Fig. 6). The latter transition is specific to $DyMn_2O_5$. Recently, the magnetic structures of $DyMn_2O_5$ at ambient pressure have been clarified by some of us thanks to single-crystal measurements [37], suggesting the strong influence of the Dy anisotropy, and the impact of the

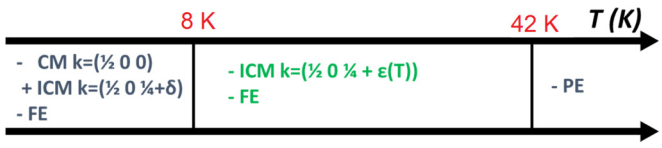

FIG. 6. $DyMn_2O_5$. Sequence of phases with temperature as described in Ref. [34]. Between 8 and 42 K commensurate ($\epsilon = 0$) and incommensurate ($\epsilon = \pm 0.015$) phases are very close to each other. They evolve differently on cooling and warming.

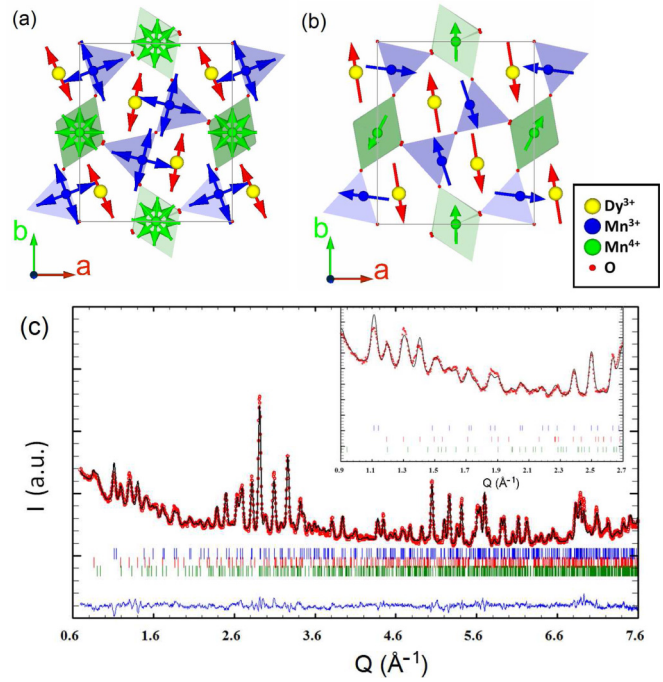

FIG. 7. $DyMn_2O_5$ at ambient pressure. (a) Magnetic structure with $\mathbf{k}_1 = (\frac{1}{2}\,0\,\frac{1}{4})$ taken from Ref. [37]; (b) magnetic structure with $\mathbf{k}_2 = (\frac{1}{2}\,0\,0)$; (c) powder magnetic pattern measured at 3.5 K. The pattern is refined by assuming the coexistence of the two phases described in (a) and (b). The solid black line is a FULLPROF refinement; the tick marks show the Bragg peak positions for the structural (blue), CM (red), and ICM (green) phases. The solid blue line is the difference between the calculated and the measured patterns. In the inset: zoom on the low-Q area.

$3d$-$4f$ exchange. According to these results and to crystal-field calculations, the Dy^{3+} anisotropy axis locates on the (a,b) plane, close to the b axis. In Ref. [37], the ICM structure is described as follows [Fig. 7(a)]. The Mn^{4+} spins rotate by 45° from site to site along c and by 90° for the Mn^{3+} spins. The Dy^{3+} spins align along the b axis with a $++--$ stacking along c. The strong easy axis anisotropy of the Dy^{3+} spins competes with the ICM spiral order and maintains the Dy spins along the b axis. The $++--$ arrangement of the Dy^{3+} spins also minimizes the Heisenberg energy term associated with the AF exchange interaction J_6 between Dy^{3+} and Mn^{3+} moments (see the discussion below). For the sites where the Mn^{3+} moments align along b, this term is fully satisfied, whereas for the sites where the Mn^{3+} moments align along a it is zero. The CM structure with $\mathbf{k}_2 = (\frac{1}{2}\,0\,0)$ is a quasicollinear structure where all Mn^{4+}, half of the Mn^{3+}, and all Dy^{3+} moments align antiparallel along b, satisfying the Dy anisotropy and R-Mn exchange terms at the expense of the Mn-Mn exchange interactions terms which favor the spiral order.

We refined the high-resolution powder pattern measured at ambient pressure and 3.5 K according to the above scheme. We obtained a good refinement by assuming that the two phases with $\mathbf{k}_1 = (\frac{1}{2}\,0\,\frac{1}{4})$ (here the incommensurate parameter was neglected) and $\mathbf{k}_2 = (\frac{1}{2}\,0\,0)$, deduced from single-crystal refinements at 15 and 2 K, respectively, coexist in the powder sample at 3.5 K [see Figs. 7(a), 7(b), 7(c)]. For the CM phase,

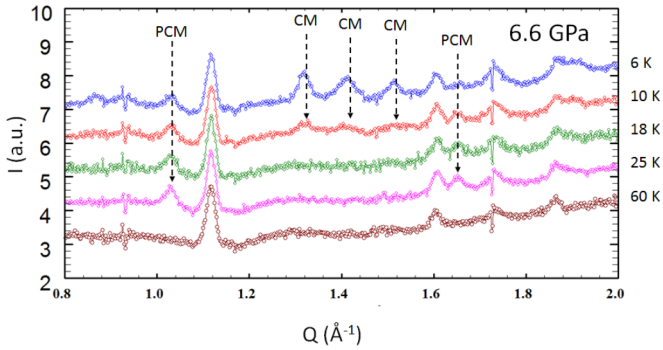

FIG. 8. $DyMn_2O_5$ neutron-diffraction patterns at 6.6 GPa for several temperatures.

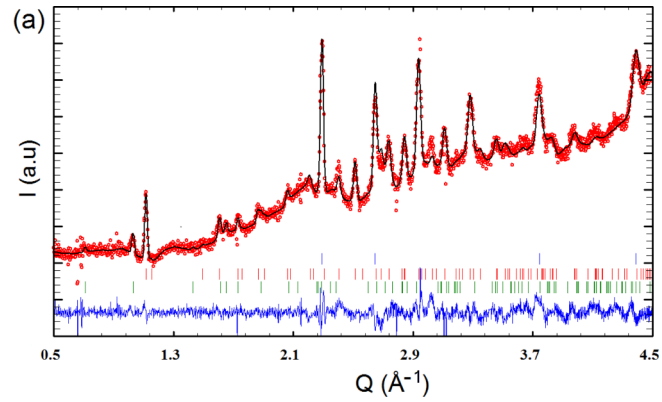

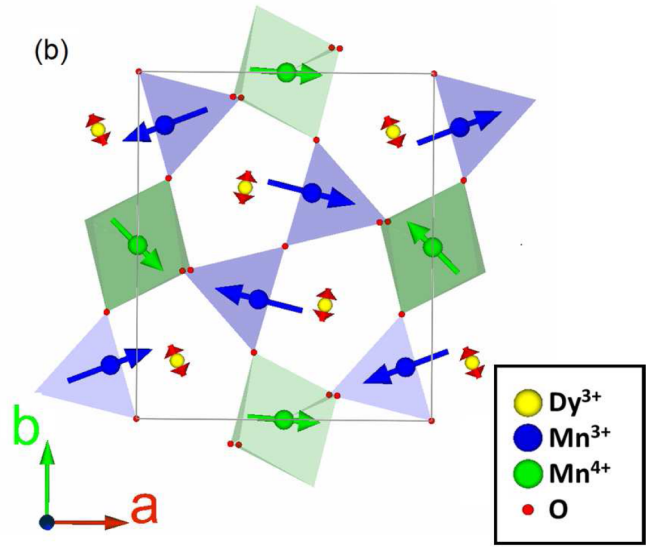

FIG. 9. $DyMn_2O_5$. (a) Refined pattern at 6.6 GPa and 18 K assuming a planar model. Red ticks: structural peaks; green ticks: magnetic peak. The blue ticks mark the position of the Pb structural peaks used to probe the pressure. (b) PCM structure: Mn^{3+} moments: blue arrows; Mn^{4+} moments: green arrows; and Dy^{3+} moments: red arrows. For the sake of clarity the Dy arrows were increased by a factor of 3.

the refinement of Dy and Mn moments (amplitudes and orientations) yields a very similar arrangement [Fig. 7(b)] as in the single crystal yet with a reduced Dy moment. Due to the phase mixture and peak overlap, we did not refine the ICM phase. Since the single-crystal magnetic structures fit our powder data quite well, we used them as a starting point to analyze the influence of pressure.

At 2.4 GPa, the neutron patterns are similar to those at ambient pressure. The ICM phase is stabilized between about 40 and 10 K, and the CM one is stabilized below 6 K. No PCM phase is observed. At 6.6 GPa, reflections associated with the PCM phase with $\mathbf{k} = (\frac{1}{2}\ 0\ \frac{1}{2})$ are observed between 40 and 10 K, whereas those of the ICM phase have totally disappeared (Fig. 8). Thus in $DyMn_2O_5$ the new PCM phase takes the place of the ICM phase as for $TbMn_2O_5$. However, as a specific feature, in $DyMn_2O_5$ the CM phase emerges below 8 K and grows at the expense of the PCM phase when the temperature further decreases (Fig. 8).

The magnetic structure of the PCM phase was refined at 18 K and 6.6 GPa where it exists as a single phase [Fig. 9(a)] using the same method as for the $TbMn_2O_5$ sample. We consider planar structures, an assumption even more justified by the strong Ising anisotropy of the Dy moments close to the b axis. The best structure [Fig. 9(b), see the Supplemental Material [32] for details] was obtained starting with the (a,b) planar structure of the ICM phase of $DyMn_2O_5$ and by refining only the moment values for Mn^{3+}, Mn^{4+}, and Dy^{3+}. As shown in Figs. 9(a), 9(b) this structure fits well the data and shows the same AF zigzag chains close to the a axis as in $TbMn_2O_5$. Moreover the moment values of 2.2 μ_B (Mn^{3+}), 1.8 μ_B (Mn^{4+}), and 0.4 μ_B (Dy^{3+}) have the right order of magnitude and obey the ordered sequence expected at this intermediate temperature. Rotating the moments orientations has little influence on the fit quality.

Under pressure, the CM phase with $\mathbf{k}_2 = (\frac{1}{2}\ 0\ 0)$ is difficult to refine because it always coexists with another magnetic phase yielding overlapping reflections. We find, however, that the ambient pressure CM structure fits the 6-K data at 2.4 and 6.6 GPa quite well if one reduces the amplitude of the Dy^{3+} and Mn^{3+} moments and increases that of the Mn^{4+} moments. Similarly, the ambient pressure ICM structure fits well the ICM phase at 2.4 GPa. The ratio between the ICM phase and the CM phase at this pressure is around 85%:15%.

IV. DISCUSSION

The main result of our experiments is the observation of a pressure-induced PCM phase with propagation vector $\mathbf{k} = (\frac{1}{2}\ 0\ \frac{1}{2})$ in $DyMn_2O_5$ and $TbMn_2O_5$ despite their different propagation vectors at ambient pressure. Being also observed in YMn_2O_5 and in $PrMn_2O_5$ under high pressure [24], such periodicity most likely corresponds to a high-pressure ground state which is generic in the RMn_2O_5 family. Assuming a planar structure, we find that the PCM phase must be associated with a lowering of symmetry along the c axis to the $P1$ SG (see the Supplemental Material [32]). Although undetectable, such symmetry lowering could play a role to relieve the frustration of the R-Mn exchange. Among the most plausible pressure-induced magnetic structures, the Tb and Dy moments are orientated along their easy axis on the (a,b) plane to minimize the rare-earth anisotropy. In $TbMn_2O_5$ this corresponds to a noticeable reorientation of the Tb moments under pressure.

The progressive onset of the PCM phase can be seen on the temperature-pressure phase diagrams, drawn in Fig. 10 by

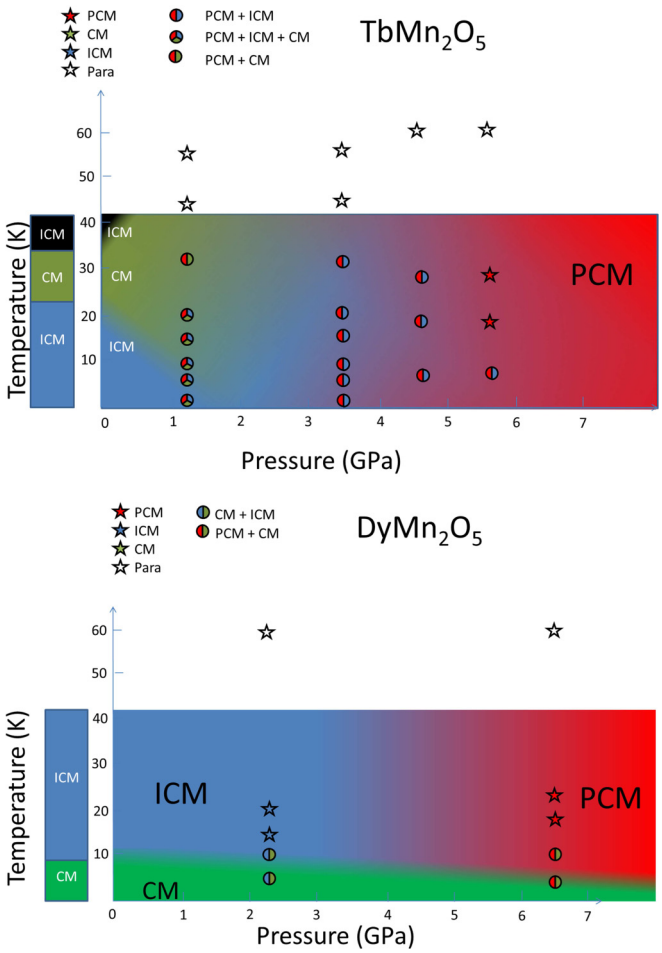

FIG. 10. Temperature-pressure phase diagrams for $TbMn_2O_5$ (top) and $DyMn_2O_5$ (bottom) deduced from the neutron data. The colored circles show the temperature-pressure data points and the coexistence of the magnetic phases. The phases of amounts less than 10% have been discarded. The rectangles on the left show the ambient pressure states.

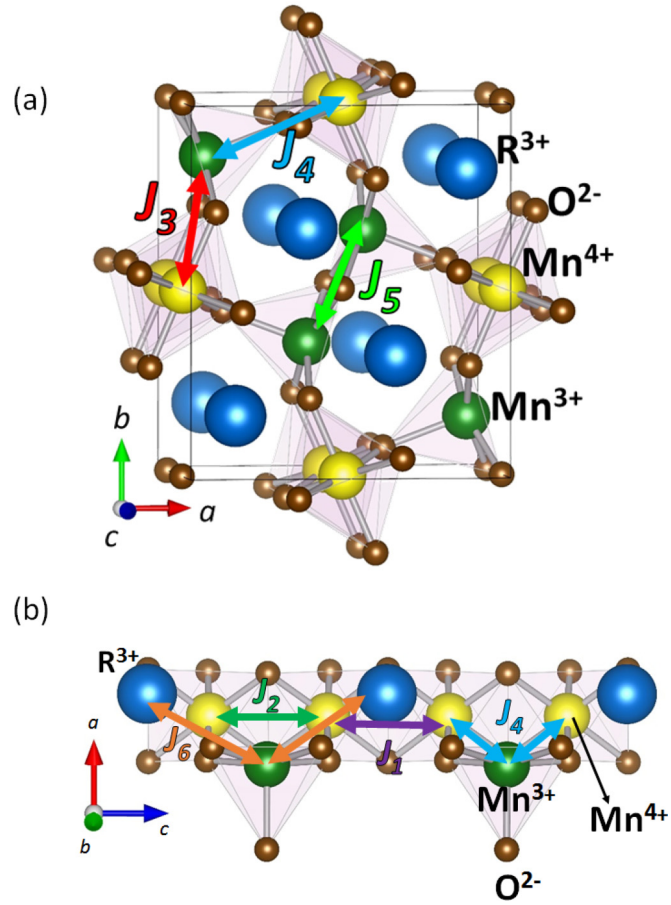

FIG. 11. Scheme of the different magnetic interactions in RMn_2O_5.

taking into account all measured pressure and temperatures (see the Supplemental Material [32]). Since in most cases, several magnetic phases coexist in the studied (P,T) range, one cannot draw well-defined transition lines. The background colors reflect the evolution of the relative weights of the different phases in a semiquantitative way. These phase diagrams involve a much higher-pressure range than those deduced from electric polarizability measurements [21] which were limited to 1.2 GPa, and the regions of coexistence are wider. The neutron data also bring extra information. In $TbMn_2O_5$ the polarizability experiments could not distinguish between the PCM and the CM phases, whereas in $DyMn_2O_5$, the PCM phase is likely connected with the mysterious paraelectric X phase found in Ref. [21].

The phase diagrams show specific features, different for the two compounds and related to their different ambient pressure states. It means that the mechanisms stabilizing the high-pressure PCM phase should be slightly different. In the following, a possible scenario is proposed. It is based on Heisenberg exchange couplings among Mn spins and taking into account the interaction scheme generally assumed for the RMn_2O_5 family with the five exchange interactions (J_1-J_5) shown in Fig. 11. Furthermore, a sixth exchange interaction is introduced, corresponding to the Heisenberg R-Mn ($3d$-$4f$) coupling. Finally, the Ising-like anisotropy of the R ions is taken into account as a single-ion anisotropy term $-D\sigma^2$, where σ is the modulus of the rare-earth-ordered moment and D is a positive constant. Note that at the mean-field level, σ should depend on the (local) molecular field H_R created on the R site by the $3d$-$4f$ coupling. It should also be strongly temperature dependent as is usually the case for rare-earth ions.

With this reasoning, it is further assumed that J_5 and J_4 are the strongest couplings. As a result, the antiferromagnetic arrangement of the zigzag chains Mn^{4+}-Mn^{3+}-Mn^{3+}-Mn^{4+} along the a axis is never called into question, yielding $k_x = 1/2$ and $k_y = 0$. Note that this is consistent with the fact that those propagation vector components persist throughout the (T,P) phase diagram. This allows to simplify the magnetic structures discussed so far in this paper as chains of Mn^{4+}, Mn^{3+}, and R moments running along the c axis and represented schematically in Fig. 12. We outline that this mapping of the real structures to 1D chains is of course a simplification, but it allows focusing on the stacking along z and thus on k_z. At the level of the simple modeling we aim to build, J_4 and J_5 are replaced by an effective Mn^{4+}-Mn^{3+} interaction called hereafter J. S is the modulus of the Mn moment, assumed here to be the same for Mn^{4+} and Mn^{3+} ions. We also assume that the J_6 exchange

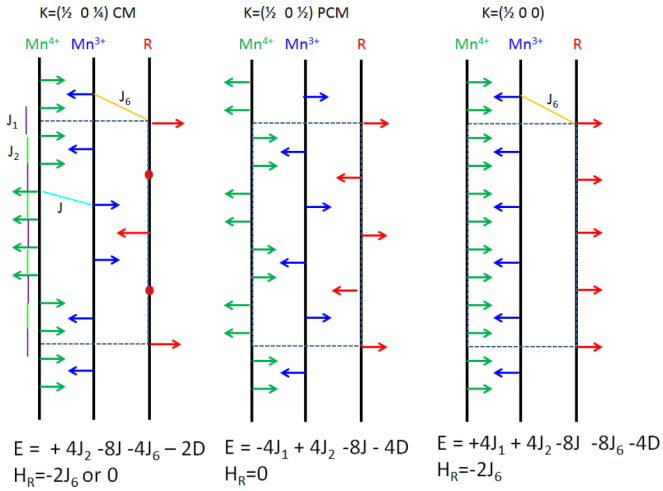

FIG. 12. One-dimensional (1D) chains which schematically represent the $R\mathrm{Mn_2O_5}$ structure along the c axis and illustrate the energy gains for different components k_z of the propagation vector. In the simplified expressions of the energy, we consider Ising spins of unit length oriented along a given axis of the (a,b) plane, which coincides with the uniaxial anisotropy axis of the R ion. H_R is proportional to the molecular field on the R site.

term concerns the R-$\mathrm{Mn^{3+}}$ interaction only [38]. A similar modeling could be developed by considering also R-$\mathrm{Mn^{4+}}$ interactions. A positive sign is taken for AF interactions.

Using these assumptions, we have calculated the energies of the three types of stacking (with $k_z = 0$, $\frac{1}{4}$, and $\frac{1}{2}$) considered in this paper (see Fig. 11),

$$\text{CM} \quad k_z = 1/4 \; \mathcal{E} = (+4J_2 - 8J)S^2 - 4J_6 S\sigma - 2D\sigma^2, \quad (1)$$

$$\text{PCM} \; k_z = 1/2 \; \mathcal{E} = (-4J_1 + 4J_2 - 8J)S^2 - 4D\sigma^2, \quad (2)$$

$$\text{CM} \quad k_z = 0 \quad \mathcal{E} = (4J_1 + 4J_2 - 8J)S^2 - 8J_6 S\sigma - 4D\sigma^2. \quad (3)$$

Importantly, it is found that the contributions of J_2 and J are identical for the different structures. The J interaction is dominant in all cases. The arrangement of two neighboring $\mathrm{Mn^{4+}}$'s across a $\mathrm{Mn^{3+}}$ layer is then always (nearly) ferromagnetic, giving systematically a $+4J_2$ contribution. Note that the same effect would be expected in the case of a ferromagnetic J_2.

We thus anticipate that the stability of the various phases observed in this oxide family results from delicate compromises involving J_1, J_6, and the anisotropy constant D of the R ion. This competition governs the stacking along the c axis, and, in turn, the z component of the propagation vector k_z. As shown in Fig. 12, compared to the $k_z = \frac{1}{4}$ case, the $k_z = \frac{1}{2}$ and $k_z = 0$ ones allow a gain in terms of R anisotropy. However, the $k_z = 0$ case is favored by a strong J_6 and by a large R magnetic moment, whereas the $k_z = \frac{1}{2}$ case is favored by a strong J_1 to the detriment of J_6. We thus speculate that pressure would reinforce J_1, hence, favoring the $k_z = \frac{1}{2}$ stacking, whereas a large R magnetic moment (as for Dy) would favor the $k_z = 0$ stacking.

In the pressure-induced phases, where the R moment is sandwiched between an AF pair of $\mathrm{Mn^{3+}}$ or $\mathrm{Mn^{4+}}$ spins, the J_6 interaction is always frustrated and cancels in Eq. (2). One could speculate that the symmetry lowering along c (see the Supplemental Material [32]), associated with a small shift of the position of the R ions, relieves this frustration thanks to the spin-lattice coupling. In this picture the degenerated J_6 interaction would be replaced by J_{6+} and J_{6-} interactions with different values.

This simple model also explains qualitatively why the pressure phase diagrams of $\mathrm{TbMn_2O_5}$ and $\mathrm{DyMn_2O_5}$ are different. In $\mathrm{TbMn_2O_5}$, the PCM phase takes the place of the ICM and CM phases with close characteristics, and the influence of temperature is not crucial. In $\mathrm{DyMn_2O_5}$ with a stronger Dy moment, the PCM phase takes the place of the ICM phase in the intermediate-temperature range, but the $k_z = 0$ ambient pressure phase remains stable at low temperatures over a large pressure range to minimize the anisotropy term. Our results suggest that, in $\mathrm{DyMn_2O_5}$, the PCM phase, likely connected with the paraelectric X phase found in Ref. [21], will become the magnetic ground state under very high pressure.

Finally we recall that in the $R\mathrm{Mn_2O_5}$ compounds where the R moment is either weak (Pr) or zero (Y), the role of J_6 in the energy balance is taken by the interaction J' between next-nearest-neighbor Mn moments and/or by antisymmetric Dzyaloshinskii-Moryia interactions [13]. Under pressure, the enhancement of J_1 with respect to J' can also explain the stabilization of the PCM phase in such cases.

V. CONCLUSION

The magnetic structure with propagation vector $(\frac{1}{2}\,0\,\frac{1}{2})$ previously observed under pressure in $\mathrm{YMn_2O_5}$ and $\mathrm{PrMn_2O_5}$ also appears in $\mathrm{TbMn_2O_5}$ and $\mathrm{DyMn_2O_5}$ under pressure. Its stabilization can be explained if the Mn-Mn interaction J_1 is reinforced with respect to the other Mn-Mn interactions. It yields a unique periodicity of the high-pressure ground-state magnetic structure in the $R\mathrm{Mn_2O_5}$ family. At ambient and low pressures, features specific to the rare earth play a role. The different ambient pressure states and magnetic phase diagram result from a subtle energy balance among J_1, the anisotropy constant D of the R ion, and the R-Mn exchange J_6. The proposed high-pressure magnetic structures also involve a symmetry lowering lifting the degeneracy of the R-Mn exchange and relieving the frustration thanks to the magnetoelastic coupling. X-ray synchrotron measurements under pressure could possibly check the proposed scenario.

ACKNOWLEDGMENTS

We are deeply thankful to O. L. Makarova for her precious help in the high-pressure experiments on $\mathrm{TbMn_2O_5}$ at LLB. We also thank S. Kichanov for his help during the initial measurements at LLB and B. Annighoefer for his help with the piston-cylinder pressure cell. We thank C. V. Colin for preliminary measurements on D1b. The postdoctoral training of M.D. was funded by the French Project ANR (DYMAGE) and Triangle de la Physique, Contract No. 2012-042T-Helix. A public grant from the Laboratoire d'Excellence Physics Atom Light Mater (Labex PALM) was overseen by the French National Research Agency (ANR) as part of the Investissements d'Avenir program (Grant No. ANR-10-LABX-0039-PALM). This work was supported by the Chinese Scholarship Council.

[1] S.-W. Cheong and M. Mostovoy, Nat. Mater. **6**, 13 (2007).

[2] H. Katsura, N. Nagaosa, and A. V. Balatsky, Phys. Rev. Lett. **95**, 057205 (2005).

[3] L. C. Chapon, G. R. Blake, M. J. Gutmann, S. Park, N. Hur, P. G. Radaelli, and S.-W. Cheong, Phys. Rev. Lett. **93**, 177402 (2004).

[4] J. J. Betouras, G. Giovannetti, and J. van den Brink, Phys. Rev. Lett. **98**, 257602 (2007).

[5] J.-H. Kim, S.-H. Lee, S. I. Park, M. Kenzelmann, A. B. Harris, J. Schefer, J.-H. Chung, C. F. Majkrzak, M. Takeda, S. Wakimoto, S. Y. Park, S.-W. Cheong, M. Matsuda, H. Kimura, Y. Noda, and K. Kakurai, Phys. Rev. B **78**, 245115 (2008).

[6] S. Wakimoto, H. Kimura, Y. Sakamoto, M. Fukunaga, Y. Noda, M. Takeda, and K. Kakurai, Phys. Rev. B **88**, 140403 (2013).

[7] S. Partzsch, S. B. Wilkins, J. P. Hill, E. Schierle, E. Weschke, D. Souptel, B. Büchner, and J. Geck, Phys. Rev. Lett. **107**, 057201 (2011).

[8] V. Balédent, S. Chattopadhyay, P. Fertey, M. B. Lepetit, M. Greenblatt, B. Wanklyn, F. O. Saouma, J. I. Jang, and P. Foury-Leylekian, Phys. Rev. Lett. **114**, 117601 (2015).

[9] I. A. Zobkalo, S. V. Gavrilov, A. Sazonov, and V. Hutanu, J. Phys.: Condens. Matter **30**, 205804 (2018).

[10] G. Yahia, F. Damay, S. Chattopadhyay, V. Balédent, W. Peng, E. Elkaim, M. Whitaker, M. Greenblatt, M.-B. Lepetit, and P. Foury-Leylekian, Phys. Rev. B **95**, 184112 (2017).

[11] G. Yahia, F. Damay, S. Chattopadhyay, V. Balédent, W. Peng, S. W. Kim, M. Greenblatt, M.-B. Lepetit, and P. Foury-Leylekian, Phys. Rev. B **97**, 085128 (2018).

[12] S. Chattopadhyay, V. Balédent, F. Damay, A. Gukasov, E. Moshopoulou, P. Auban-Senzier, C. Pasquier, G. André, F. Porcher, E. Elkaim, C. Doubrovsky, M. Greenblatt, and P. Foury-Leylekian, Phys. Rev. B **93**, 104406 (2016).

[13] P. G. Radaelli and L. C. Chapon, J. Phys.: Condens. Matter **20**, 434213 (2008).

[14] Y. Noda, H. Kimura, M. Fukunaga, S. Kobayashi, I. Kagomiya, and K. Kohn, J. Phys.: Condens. Matter **20**, 434206 (2008).

[15] P. G. Radaelli, C. Vecchini, L. C. Chapon, P. J. Brown, S. Park, and S.-W. Cheong, Phys. Rev. B **79**, 020404 (2009).

[16] R. P. Chaudhury, C. R. dela Cruz, B. Lorenz, Y. Sun, C.-W. Chu, S. Park, and S.-W. Cheong, Phys. Rev. B **77**, 220104(R) (2008).

[17] C. Wilkinson, P. J. Brown, and T. Chatterji, Phys. Rev. B **84**, 224422 (2011).

[18] S. Petit, V. Baledent, C. Doubrovsky, M. B. Lepetit, M. Greenblatt, B. Wanklyn, and P. Foury-Leylekian, Phys. Rev. B **87**, 140301 (2013).

[19] J.-H. Kim, M. A. van der Vegte, A. Scaramucci, S. Artyukhin, J.-H. Chung, S. Park, S.-W. Cheong, M. Mostovoy, and S.-H. Lee, Phys. Rev. Lett. **107**, 097401 (2011).

[20] G. R. Blake, L. C. Chapon, P. G. Radaelli, S. Park, N. Hur, S.-W. Cheong, and J. Rodríguez-Carvajal, Phys. Rev. B **71**, 214402 (2005).

[21] C. R. dela Cruz, B. Lorenz, Y. Y. Sun, Y. Wang, S. Park, S.-W. Cheong, M. M. Gospodinov, and C. W. Chu, Phys. Rev. B **76**, 174106 (2007).

[22] M. Deutsch, T. C. Hansen, M. T. Fernandez-Diaz, A. Forget, D. Colson, F. Porcher, and I. Mirebeau, Phys. Rev. B **92**, 060410 (2015).

[23] D. P. Kozlenko, N. T. Dang, S. E. Kichanov, E. V. Lukin, A. M. Pashayev, A. I. Mammadov, S. H. Jabarov, L. S. Dubrovinsky, H.-P. Liermann, W. Morgenroth, R. Z. Mehdiyeva, V. G. Smotrakov, and B. N. Savenko, Phys. Rev. B **92**, 134409 (2015).

[24] W. Peng, V. Balédent, S. Chattopadhyay, M.-B. Lepetit, G. Yahia, C. V. Colin, M. J. Gooch, C. R. Pasquier, P. Auban-Senzier, M. Greenblatt, and P. Foury-Leylekian, Phys. Rev. B **96**, 054418 (2017).

[25] C. Doubrovsky, G. André, A. Gukasov, P. Auban-Senzier, C. R. Pasquier, E. Elkaim, M. Li, M. Greenblatt, F. Damay, and P. Foury-Leylekian, Phys. Rev. B **86**, 174417 (2012).

[26] J. Alonso, M. Casais, M. Martínez-Lope, J. Martínez, and M. Fernández-Díaz, J. Phys.: Condens. Matter **9**, 8515 (1997).

[27] I. N. Goncharenko, High Press. Res. **24**, 193 (2004).

[28] M. Deutsch, V. Baledent, M. T. Fernandez-Diaz, P. Foury-Leylekian, T. Hansen, I. Mirebeau, W. Peng, and S. Petit, Neutron study of the new pressure induced commensurate phase in RMn2O5 multiferroics. Institut Laue-Langevin (ILL) 10.5291/ILL-DATA.5-31-2446 (2016).

[29] S. Klotz, *Techniques in High Pressure Neutron Scattering* (CRC Press, Boca Raton, FL, 2012).

[30] S. Klotz, L. Paumier, G. L. March, and P. Munsch, High Press. Res. **29**, 649 (2009).

[31] J. Rodriguez-Carvajal, Physica B: Condens. Matter **192**, 55 (1993).

[32] See Supplemental Material at http://link.aps.org/supplemental/10.1103/PhysRevB.98.024408 for details about the crystal structure, estimation of the phase ratio, symmetry analysis, and temperature dependence of the neutron patterns under pressure.

[33] P. P. Gardner, C. Wilkinson, J. B. Forsyth, and B. M. Wanklyn, J. Phys. C: Solid State Phys. **21**, 5653 (1988).

[34] W. Ratcliff, V. Kiryukhin, M. Kenzelmann, S.-H. Lee, R. Erwin, J. Schefer, N. Hur, S. Park, and S.-W. Cheong, Phys. Rev. B **72**, 060407 (2005).

[35] C. Wilkinson, F. Sinclair, P. Gardner, J. Forsyth, and B. Wanklyn, J. Phys. C: Solid State Phys. **14**, 1671 (1981).

[36] J. M. Liu and S. Dong, J. Adv. Dielectr. **05**, 1530003 (2015).

[37] S. Chattopadhyay, S. Petit, E. Ressouche, S. Raymond, V. Balédent, G. Yahia, W. Peng, J. Robert, M.-B. Lepetit, M. Greenblatt, and P. Foury-Leylekian, Sci. Rep. **7**, 14506 (2017).

[38] Even though one can *a priori* assume five different values of J_6 according to the Mn ions connected with the the rare earth, we will use an average value here. Indeed, without further investigation it is impossible to have a precise idea of the different J_6 values.